Molecular anisotropy and rearrangement as mechanisms of toughness and extensibility in entangled physical gels

Chelsea E. R. Edwards, Danielle J. Mai, Shengchang Tang, and Bradley D. Olsen

Phys. Rev. Materials **4**, 015602 — Published 27 January 2020

DOI: 10.1103/PhysRevMaterials.4.015602

Molecular anisotropy and rearrangement as mechanisms of toughness and extensibility in entangled physical gels

Chelsea E. R. Edwards,[†] Danielle J. Mai,[†] Shengchang Tang, and Bradley D. Olsen*
Department of Chemical Engineering, Massachusetts Institute of Technology, Cambridge, MA 02139 USA

(Received 4 September 2019)

ABSTRACT

Dynamic networks formed by physically crosslinked, entangled polymers have emerged as self-healing, stretchable, and functional materials. Entangled associative gels with remarkable toughness and extensibility have been produced by several distinct chemical approaches, suggesting that these enhanced mechanical properties result from molecular-scale topology. Previously, artificially engineered associative proteins were designed to provide an ideal model system to investigate the role of entanglement on gel mechanics via well-defined entangled or unentangled physical gels. Herein, uniaxial strain-induced structural changes in these model gels were observed using *in situ* small-angle X-ray scattering (SAXS) and *in situ* polarized optical microscopy (POM) up to 2,000% engineering strain. Anisotropic optical responses to uniaxial strain at the nano-, micro-, and macro- scales suggest that stress dissipation mechanisms enable high extensibility and toughness. Nano- and microscopic anisotropy observed by SAXS indicate stretching and alignment of flexible polymer strands along the straining axis, and non-monotonic macroscopic anisotropy observed by POM suggests relaxation within the hydrogel due to rearrangement of associative network junctions. Unentangled hydrogels exhibit low toughness and a strain-rate-dependent transition from ductile to brittle tensile behavior, which is typical for associative polymer solutions. These findings indicate that topological entanglements and the freedom of individual chains to align at the nanoscale due to junction relaxation are both critical to achieving high toughness and elongation in entangled physical gels.

[†]These authors contributed equally. *Corresponding author: bdolsen@mit.edu

I. INTRODUCTION

Physically crosslinked polymer networks have generated broad interest as self-healing soft materials [1-4], but noncovalent networks are generally susceptible to erosion, creep, and mechanical failure [5-9]. Much effort has been devoted to improving the stability of polymer networks for use in chemically and physically demanding applications including stretchable electronics [10,11], biomimetic elastomers [12-18], and injectable biomaterials [19-21]. In polymer networks and gels, mechanical properties such as toughness and extensibility have been improved using a generally accepted strategy of building energy dissipation mechanisms into networks that maintain elasticity [5,22,23]. Distributing stress prevents the propagation of cracks and defects that may lead to gel fracture, and typical dissipative mechanisms include dynamic bonding via hydrophobic interactions [8,9], hydrogen bonding [10,17], ionic interactions [11], metal–ligand coordination [12-15], or guest–host complexation [18]. Tough gels and networks maintain structural integrity using elastic mechanisms such as high functionality crosslinks [13-15], responsive reinforcing domains [16,19], or double networks [22].

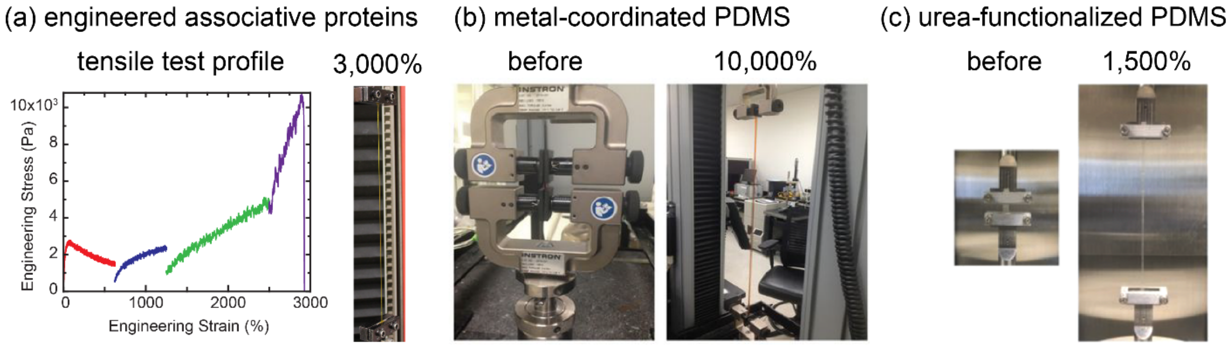

FIG. 1. High toughness and extensibility of physical polymer networks with distinct chemical features. Images adapted by permission from (a) *Macromolecules*: Oxidatively Responsive Chain Extension to Entangle Engineered Protein Hydrogels by S. Tang, M. J. Glassman, S. Li, S. Socrate, and B. D. Olsen. Copyright (2014) American Chemical Society; (b) Springer, *Nature Chemistry*: A highly stretchable autonomous self-healing elastomer by C.-H. Li, *et al.* (2016); and (c) John Wiley & Sons, *Advanced Functional Materials*: Superstretchable, Self□Healing Polymeric Elastomers with Tunable Properties by P.□F. Cao, *et al.* (2018).

Recently, topological entanglement was used to toughen physical polymer networks composed of either artificially engineered proteins with associative domains [20], polydimethylsiloxane (PDMS) with metal–ligand coordination [12], or PDMS with supramolecular hydrogen bonding [17]. In each system, high molecular weight polymers with numerous physical crosslinking domains were produced by condensation of telechelic associative polymers. All of the resulting polymer networks exhibited high toughness and elongation at break (> 3,000% fracture strains, FIG. 1), as well as the ability to self-heal at room temperature in the absence of external stimuli [12,17,20]. The similar physical responses of chemically disparate materials suggest that polymer topology and entanglement have a strong and general effect on the toughness and extensibility of physically crosslinked polymer networks.

Engineered protein-based materials provide a well-defined system to investigate the role of topological entanglement on the toughness and extensibility of physical polymer networks. Genetic engineering allows for the facile development of polymeric materials with precise molecular weights [24,25], specific amino acid sequences that provide intrinsic function (*e.g.* binding interactions and molecular recognition) [26-29], and self-assembling domains that form higher order structures [8,9,30-35]. A widely studied family of protein-based physical gels combines flexible spacers with associative coiled-coil domains [6-9,33-41] to produce such model associative networks. In this work, model unentangled and entangled protein networks comprise alternating flexible spacer domains (hereafter denoted C_{10}) and pentamer-forming coiled-coil domains (denoted P) [20,35-37].

Flexible C_{10} spacers comprise ten repeats of the nonapeptide -ProGluGly(AlaGly)$_3$-, which have been shown to form water-soluble polyelectrolyte coils [9,41,42]. Proline is known to disrupt chain folding [43,44], and the inclusion of proline in the nonapeptide motif is hypothesized to frustrate packing of hydrophobic alanylglycine repeats [41]. Charged glutamic acid residues improve water solubility, and glycine residues impart flexibility in the backbone chain [44,45]. The random coil character of a single C_{10} protein domain was confirmed by circular dichroism spectroscopy [9].

Physical crosslinking is achieved using secondary structural elements of proteins, such as coiled-coil motifs formed by the association of two or more α-helical coils. Each α-helix consists of periodic amino acid heptads referred to as *abcdefg* [46,47]. Interactions between hydrophobic residues in positions *a* and *d* and charged residues in positions *e* and *g* drive association, and the amino acid sequence and chain length can be modified to tune the directionality, specificity, aggregation number, and higher-order structures [46-51]. Associative coiled coils typically have free energies ranging from 12–55 kJ/mol [49-51], which are an order of magnitude weaker than protein backbone bonds (typical dissociation energies of C–C and C–N bonds are 345 and 305 kJ/mol, respectively [52]).The coiled-coil domain in this work has an association free energy of 18 kJ/mol [51]. This pentamer-forming domain was selected because coiled-coil bundles with odd aggregation numbers have been shown to suppress erosion in physical protein gels [6].

Model associative proteins with reactive end groups enabled the synthesis of high-molecular-weight species that form topological entanglements, leading to the early discovery of high toughness and extensibility in entangled physical networks [20]. Previously, unentangled associative proteins ($C_{10}(PC_{10})_4$, FIG. 2a) were genetically modified to include cysteine residues at both termini (cys-$C_{10}(PC_{10})_4$-cys) [35,36]. The resulting protein chains were extended by oxidatively triggered disulfide bond formation (FIG. 2b) [20,39,53]. Disulfide bonds produced

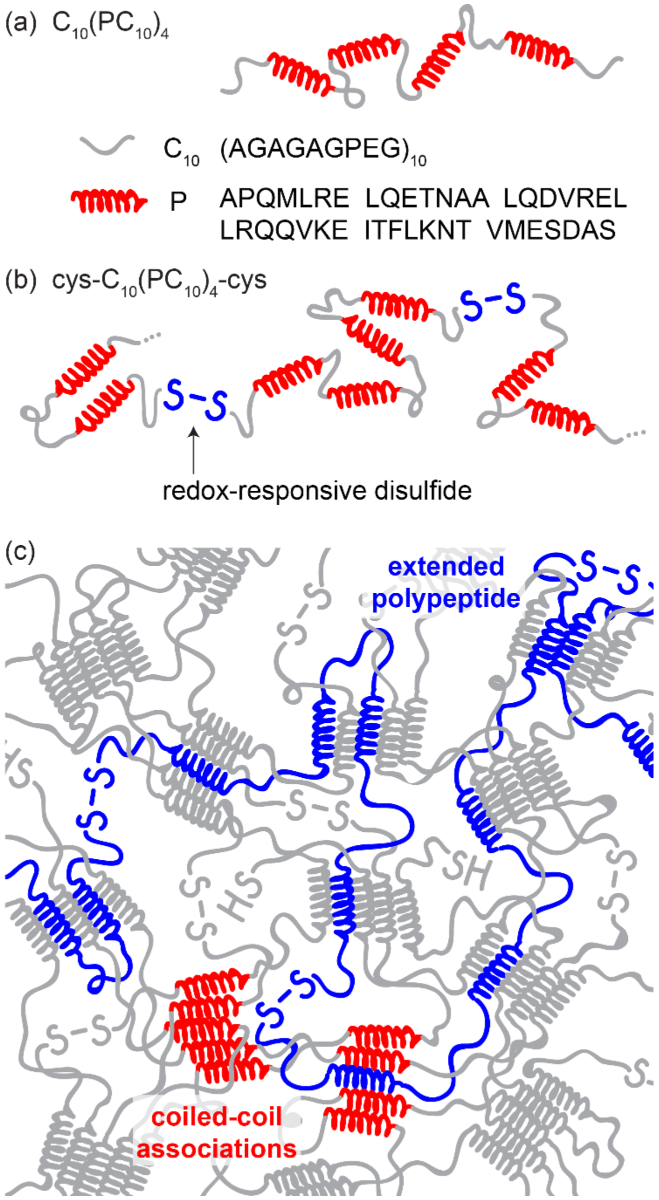

FIG. 2. Molecular design of proteins in (a) unentangled and (b) entangled physical hydrogels. Letters indicate amino acid sequences that make up flexible polyelectrolyte coils (C_{10}) and pentamer-forming associative domains (P). S–S bonds represent cysteine bridges formed during chain extension. Structures not drawn to scale. (c) Schematic of an entangled physical gel formed by chain-extended proteins.

by chain extension are an order of magnitude stronger than the associative domains that form physical crosslinks (FIG. 2c), with typical C–S and S–S bond dissociation energies of 272 and 268 kJ/mol, respectively [52]. Entangled and unentangled gels both exhibited rapid recovery of mechanical properties following the shear-induced rupture of the transient networks [7,20]. The entangled physical protein hydrogels also exhibited remarkable tensile toughness (65,000 ± 24,500 J m^{-3}) and extensibility (failure engineering strain of 2,970 ± 860%) under a designed test profile (FIG. 1a) [20]. In comparison, unentangled $C_{10}(PC_{10})_4$ hydrogels were brittle and failed immediately in the tensile apparatus. Similar observations were subsequently made on several structurally analogous systems [12,17], but a molecular explanation for the behavior remains elusive. The dramatic changes in hydrogel mechanics following chain extension suggest that molecular-scale topology has a profound effect on hydrogel nanostructure and macroscopic response during deformation.

The structural evolution and stress response of soft materials can be probed simultaneously under deformation using *in situ* techniques including small-angle scattering and polarized optical microscopy (POM). Real-time structural measurements are critical for physical gels with dynamic crosslinks in which the rate of polymer segment and network junction relaxation may exceed the rate of deformation. *In situ* small-angle scattering has been applied to investigate nanostructural dynamics in several tough physical gels, including polymer–clay nanocomposite gels [54,55] and supramolecular hydrogels [56,57] during uniaxial extension and thermoresponsive associative protein hydrogels under shear [40,58]. Generally, extensional deformation of tough gels produces anisotropic scattering, which is considered to emerge from the alignment of crosslinking domains and elongation of flexible domains. In nanocomposite blend hydrogels, anisotropic nanoplatelets oriented parallel to the stretching direction [54,55], and structural changes occurred preferentially in the polymer phase due to stretching of flexible chains [54]. In a nanophase-separated supramolecular hydrogel, contrast-variation small-angle neutron scattering (SANS) revealed the transient size, spacing, and orientation of nanodomains following a step strain to provide a detailed mechanistic view of stress relaxation by a tough hydrogel [56]. In supramolecular hydrogels, *in situ* small-angle X-ray scattering (SAXS) revealed the rate-dependent evolution of nanostructural anisotropy and nanodomain rearrangement during uniaxial elongation [57]. *In situ* POM measures birefringence to provide a relative measure of polymer chain orientation and alignment, which complements detailed nanostructural information from *in situ* SAXS. Emergent birefringence is commonly observed in polymers with liquid crystalline domains [59,60], hydrogels with flow-induced alignment [61], and polymer networks during extensional deformation [62-67].

This work investigates the role of topological entanglement on the tensile response of physically crosslinked polymer networks using *in situ* SAXS and *in situ* POM. Unentangled and entangled physical gels exhibited distinct linear viscoelastic behavior, as well as rate-dependent stress responses during uniaxial extension. Analyzing *in situ* SAXS data in the context of a broad peak scattering model revealed quantitative differences in the nanostructural evolution of unentangled and entangled hydrogels during elongation, which corresponded to changes in macroscopic structure and birefringence measured using *in situ* POM. Together, these results suggest a combination of molecular-scale mechanisms that enable the toughness and extensibility of entangled associative hydrogels.

II. MATERIALS AND METHODS

The engineered proteins $C_{10}(PC_{10})_4$ and cys-$C_{10}(PC_{10})_4$-cys were prepared as previously reported to generate well-defined unentangled and entangled hydrogels, respectively [20,35-37]. Experimental details for protein expression and purification are described in the Supplemental Material [68].

A. Chain extension reaction

Oxidative thiol coupling was used to generate high molecular weight species from cysteine-terminated associative proteins [19,20,39,53]. Purified cys-$C_{10}(PC_{10})_4$-cys proteins were dissolved to a final concentration of 10% (w/v) in a denaturing and reducing buffer containing 6 M urea, 2-fold molar excess tris(2-carboxyethyl)phosphine hydrochloride (TCEP, 6.3 mM), and 20 mM Tris (pH 8.0). Urea enhances protein solubility during chain extension reactions, and TCEP reduces terminal cysteine residues to expose free sulfhydryl groups. Protein solutions were constantly stirred for approximately 2 weeks at 4 °C, and degradation of TCEP during this period allowed protein coupling in a non-reducing environment. Chain extension reactions were monitored weekly using non-reducing sodium dodecyl sulfate polyacrylamide gel electrophoresis. After oxidation, residual salt was removed from chain-extended proteins by dialysis against ultrapure water (MilliQ, 18.2 MΩ cm), and water was removed by lyophilization. Entanglement was verified using shear rheology on hydrogels prepared from purified samples.

B. Hydrogel preparation

Associative protein hydrogels with topological entanglements (chain extended) and without entanglements ($C_{10}(PC_{10})_4$) were prepared to a final concentration of 15% (w/v) in 100 mM sodium phosphate (pH 7.6). Lyophilized proteins were hydrated overnight at 4 °C, and the resulting gels were periodically mixed with a spatula to ensure a homogeneous concentration.

Mixed samples were centrifuged for 10 minutes at 10,000 rpm to remove bubbles prior to loading in custom polytetrafluoroethylene (PTFE) molds (dog-bone shape with 1 mm gage length, 4 mm width, and 2 mm thickness). To prevent sample dehydration, PTFE molds were sandwiched between brass plates, held together with a C-clamp, wrapped in plastic film (Saran), and stored in individually sealed plastic bags containing damp paper towels. Entangled gel samples were stored at 4 °C for at least 4 days to allow stress relaxation prior to tensile testing. Unentangled gels were stored at 4 °C for at least 2 hours prior to testing.

C. Shear rheology

Frequency sweep experiments were performed on an Anton Paar MCR 702 rheometer operating in single-drive mode with a sandblasted cone–plate geometry (25 mm diameter and 1° cone angle with 48-μm truncation gap height; Peltier-temperature-controlled plate, P-PTD 200). Two days before the experiment, protein samples were hydrated at 15% (w/v) in 100 mM sodium phosphate (pH 7.6). On the day of the experiment, samples were mixed with a spatula to ensure a homogeneous concentration and centrifuged for 10 minutes at 10,000 rpm to remove bubbles before loading onto the rheometer. Hydrogel samples were trimmed at a truncation gap of 58 μm, after which the final truncation gap height was set to 48 μm. The sample edges were coated with mineral oil (Amresco) to minimize water evaporation. Humidity and temperature were further controlled using a Peltier-temperature-controlled hood (Anton Paar, H-PTD 200). Samples were heated to 90 °C and cooled to 25 °C at 5 °C/min to eliminate thermal and shear history by unfolding of coiled-coil domains at temperatures above 52 °C [9,20]. All subsequent experiments were performed at 25 °C. Linear viscoelasticity was characterized using frequency sweep experiments from 0.001–1.0 rad/s at 5% strain and 0.1–100 rad/s at 1% strain, which were confirmed to be in the linear viscoelastic regime using strain sweep experiments (0.1–10% strain at 0.01, 1.0, and 100 rad/s, details included in the Supplemental Material [68]).

D. Tensile testing

Tensile testing was performed using a Linkam TST350 temperature-controlled tensile stress stage equipped with a 20 N load cell and driven by either a T95 controller with Linksys32 (SAXS) or a T96 controller with LINK software (POM). Custom titanium clamps were added to test samples shorter than the minimum TST350 sample length, and sandpaper (80 grit) was glued to the custom clamps to improve grip. The tensile stage was aligned perpendicular to the incident beam, and the opening was aligned to allow the beam to pass through samples during *in situ* SAXS (vertical stage) or *in situ* POM (horizontal stage). The symmetric displacement of the clamps enabled observation of the same zone of the sample during extension. The engineering strain $e = (L - L_0)/L_0 \times 100\%$ was determined from the displacement of the clamps L. For all tests, the initial displacement L_0 was 3.5 ± 0.1 mm. The clamps were displaced at a constant velocity of 100 or 300 μm/s, corresponding to engineering strain rates of 0.028 and 0.084 s^{-1}, respectively. In this experimental setup, the Hencky strain rate decreases throughout the deformation [69]. The engineering stress was calculated using the initial cross-sectional area of 2 mm × 4 mm in the dog bone. Gel toughness was calculated as the area under the engineering stress–strain curve. To prevent sample dehydration during stretching, air was humidified by passage through an in-line bubbler and circulated into the sample chamber. All tensile testing was performed at 24.5 ± 0.5 °C.

E. Small-angle X-ray scattering

Using a high-flux synchrotron X-ray source, *in situ* SAXS enables the measurement of nanostructural changes in soft and biological materials during mechanical testing [40,55-58,70-

77]. SAXS experiments were conducted at beamline 7.3.3 at the Advanced Light Source at Lawrence Berkeley National Laboratory [70]. The flight tube was selected to identify nanoscale features within a q range of 0.06–2.5 nm^{-1}, where the scattering vector is $q = (4\pi/\lambda)\sin(\theta)$, given an X-ray wavelength λ of 1.2398 Å and scattering angles 2θ. Specifically, scattering was measured using a Pilatus 2M CCD detector with 0.172 mm square pixels and a sample-to-detector distance of 2.838 m. Tensile data were collected at 3.3 Hz. For stretching rates of 100 or 300 μm/s, the time elapsed between the start of each acquisition was 10.0 or 3.3 s, respectively. For each scattering pattern acquisition, the sample was exposed for 0.5 s to limit damage due to accumulated exposure to the X-ray beam [73,77].

2D scattering patterns were reduced to radial and azimuthal 1D profiles in order to quantify nanostructural changes due to anisotropic deformations. Reductions to 1D were carried out using the Nika package for Igor Pro (Wavemetrics) [78]. Raw SAXS images were first corrected for background scattering, and areas covered by the mask and beam stop were omitted to minimize the effect of flares and lines of zero intensity. Radial 1D scattering profiles were generated by averaging circular sectors of width ±10° (total width of 20°), which were centered perpendicular (0° azimuthal) and parallel (90° azimuthal) to the straining axis. Radial scattering profiles were fit to correlation length and broad peak models [79] using MATLAB. A subset of radial profiles generated from circular sector widths of ±5°, ±10°, ±15°, or ±20° showed negligible differences in fit quality or final fit parameters. Elsewhere, soft materials exhibiting anisotropic scattering under tension have been quantified using sector widths ranging from ±4° to ±30° [54-57,72-77]. Anisotropic features were quantified by producing azimuthal 1D scattering profiles from an annular q average of scattered intensity as a function of azimuthal angle φ [56,57,76,77]. This analysis was conducted by azimuthally averaging sectors every 10° (width ±5°) over a range of q

$= 0.8 \pm 0.05$ nm^{-1}, where the largest deviations were observed between the radial scattering profiles centered parallel and perpendicular to the straining axis.

F. Polarized optical microscopy

Polarized optical microscopy (POM) was performed using a Zeiss Axioplan microscope equipped with an Axiocam 503 mono camera, 2.5×/0.075 NA Epiplan-NEOFLUAR objective, sliding 360° rotatable analyzer set orthogonally to the polarizer, and a neutral-density filter (6% transmission). During birefringence measurements, samples were illuminated with plane-polarized light, and the incident light was transmitted through a cross polarizer prior to detection by the camera. The neutral-density filter was removed during birefringence measurements of unentangled hydrogels to enable detection of weaker birefringent signals, and all optical signal intensities were normalized during video processing. The TST350 stage was aligned such that the stretching direction followed a 45° angle between the crossed polarizers. Tensile and video data were collected at 20 Hz. MATLAB was used to process videos, which were corrected for initial sample transmission and dark field background and converted to power fraction I_{PF}:

$$I_{\mathrm{PF}}(t) = \frac{I_{\mathrm{sample}}(t) - I_{\mathrm{dark}}}{I_{\mathrm{trans}}(t=0)} - \frac{I_{\mathrm{cross}} - I_{\mathrm{dark}}}{I_{\mathrm{open}}} \tag{1}$$

where I_{sample} and I_{trans} are the transmitted intensities of cross- and plane-polarized light through the sample, I_{dark} is the detector background intensity, and I_{cross}, and I_{open} are the cross- and plane-polarized background intensities, respectively. Time-resolved I_{PF} was mapped to the corresponding engineering strain using strain rates calculated from the tensile data.

III. RESULTS AND DISCUSSION

A. Structure of protein-based physical gels

Small-angle X-ray scattering reveals similar quiescent structures from 1 – 100 nm in unentangled and entangled protein-based hydrogels (FIG. 3). Associative domains are considered to dominate the scattering overall [38] and produce the characteristic features of stronger scattering at low *q* and a broad scattering peak at intermediate *q*. These features are compared in 1D scattering profiles generated from radial sectors parallel and perpendicular to the tensile apparatus. The radial scattered intensity *I* as a function of the scattering vector *q* was fit to a broad peak model, which is commonly used to identify characteristic length scales in hydrogel systems with clustered domains [56,57,79,80]:

$$I(q) = \frac{A}{q^n} + \frac{C}{1+(|q-q_0|\xi)^m} + B \qquad (2)$$

Multiplicative factors *A* and *C* and exponents *m* and *n* are related to the Porod and Lorentzian functions, respectively, and *B* is background scattering. The peak position q_0 and correlation length ξ suggest relevant length scales in associative protein hydrogels, which are illustrated in

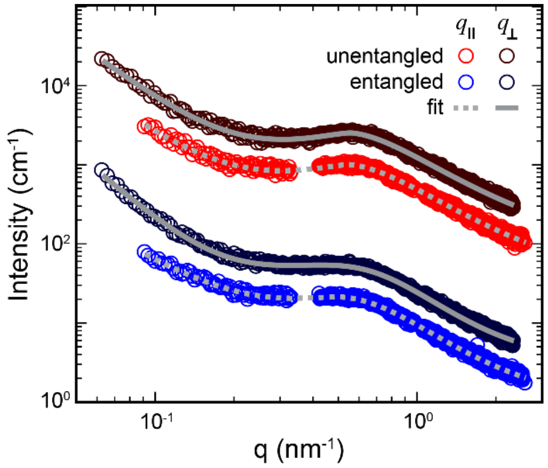

FIG. 3. Quiescent 1D radial scattering profiles reveal similarities in the isotropic structures of unentangled (red) and entangled (blue) associative protein hydrogels. Lines indicate fits to the broad peak model, and data are offset vertically for clarity.

FIG. 4 [79,81]. Broad peak model fits confirmed the isotropic nanostructure of unentangled physical gels prior to deformation. Quiescent entangled gels exhibited weakly asymmetric scattering, which is attributed to minor sample deformation during loading and alignment of the tensile apparatus. Fit parameters were averaged between both directions to quantify structural features. 1D scattering profiles were also fit to a correlation length model ($q_0 = 0$), which produced qualitatively similar results to the broad peak model as further discussed in the Supplemental Material [68].

The spatial distribution of gel domains can be quantified from the scattering peak position q_0, which corresponds to the Bragg d-spacing by the relation $d = 2\pi/q_0$. The d-spacing reflects the average center-of-mass separation between network junctions formed by pentameric bundles of associative coiled coils. In unentangled gels, each coiled-coil domain is flanked on both ends by C_{10} spacers, and the spatial extent of a pentameric bundle is estimated as the bundle size plus two hydrodynamic radii from surrounding C_{10} spacers (FIG. 4a). The spatial extent is calculated using hydrodynamic radii instead of hydrodynamic diameters to prevent double counting of C_{10} spacers; this assumption leads to an underestimation for spacers that are only attached to one coiled-coil domain instead of bridging a pair of coiled-coil domains. The coiled-coil bundle is

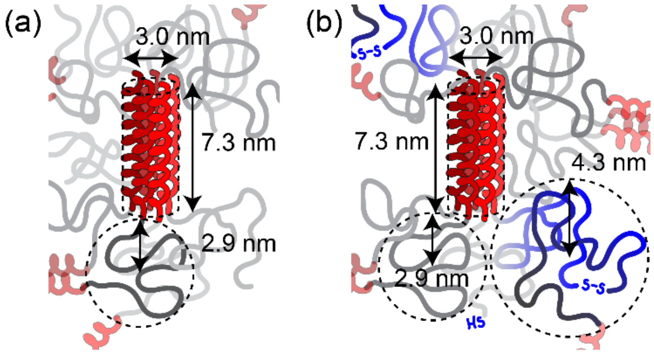

FIG. 4. Molecular dimensions of associative proteins that form (a) unentangled and (b) entangled physical hydrogels. Protein domains include pentameric coiled coil bundles (red), flexible C_{10} spacers (gray), and effective C_{20} spacers

approximated as a cylinder of diameter 3.0 nm and of length 7.3 nm [38,82]. The hydrodynamic radius of the C_{10} spacer between coiled coils is calculated as 2.9 nm from the scaling for disordered, flexible proteins, $R_H = 2.21\ N^{0.57}$ Å, where N is the number of amino acids [83]. The spatial extent of a pentameric bundle flanked by C_{10} spacers is estimated to be 13.1 nm axially (7.3 nm from the cylinder length and two contributions of 2.9 nm from C_{10} spacers on either end) or 8.8 nm radially (3.0 nm from the cylinder diameter and 2 × 2.9 nm from C_{10} spacers). Averaging these values to predict a spatial extent of 11.0 nm is consistent with the Bragg d-spacing of unentangled hydrogels, where $q_0 = 0.55 \pm 0.01$ nm^{-1} corresponds to a d-spacing of 11.4 ± 0.2 nm. For chain-extended proteins, coupling of C_{10} spacers results in effective C_{20} spacers with expanded hydrodynamic radii of 4.3 nm (FIG. 4b). The average initial peak position of 0.49 ± 0.03 nm^{-1} for entangled hydrogels corresponds to an increase in the Bragg d-spacing to 12.8 ± 0.8 nm, consistent with the presence of longer average spacers between junctions. The average quiescent correlation length ξ_0 was the same for unentangled and entangled hydrogels ($\xi_0 = 2.3 \pm 0.1$ nm), which reflects the identical local chemical features of C_{10} spacers and effective C_{20} spacers.

Despite sharing quiescent structural features, gels composed of unentangled and chain-extended proteins exhibited distinct linear viscoelastic responses (FIG. 5). In unentangled associative protein hydrogels, a crossover in the shear storage modulus (G') and loss modulus (G'') emerged at a frequency $\omega_{\text{crossover}}$ of 0.35 rad/s, which corresponds to a characteristic stress relaxation time of the hydrogel [7,20]. A maximum in G'' is attributed to the coiled-coil relaxation time. The G'' peak occurred near $\omega_{\text{crossover}}$, suggesting that the relaxation of unentangled hydrogels is closely related to rearrangement of coiled-coil domains. Below the crossover frequency, unentangled hydrogels approached terminal relaxation behavior ($G' \sim \omega^2$

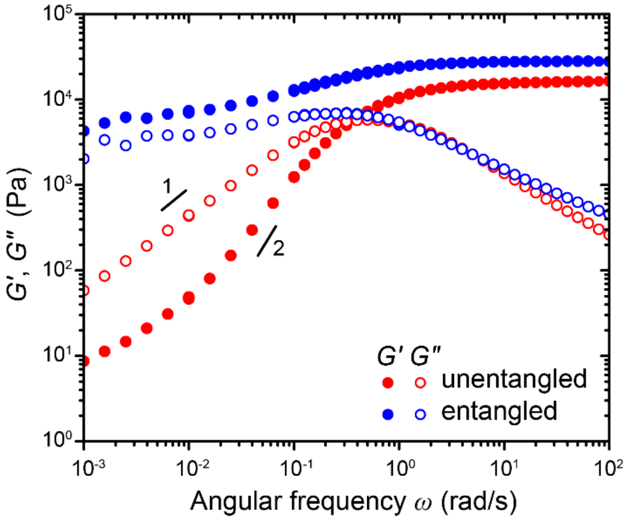

FIG. 5. Shear storage (•, G') and loss (◦, G'') moduli of unentangled (red) and chain-extended (blue) associative protein hydrogels.

and $G'' \sim \omega$), followed by a deviation in G' at frequencies below 0.01 rad/s. This low-frequency G' behavior is commonly observed in transient networks, in which physical associations such as coiled-coil aggregation, hydrogen bonding, or metal–ligand coordination may affect Rouse relaxation [20,37,84-87].

Chain-extended proteins did not exhibit a moduli crossover; instead, G' exceeded G'' across the frequency window. The lack of a moduli crossover or terminal regime suggests that entanglements form topological constraints in the gel network that prevent chain relaxation and rearrangement [20,69,84]. The high-frequency plateau modulus G'_e of chain-extended hydrogels exceeded that of unentangled hydrogels (28,100 ± 100 Pa and 16,100 ± 300 Pa, respectively; mean ± standard error from 10^1–10^2 rad/s), consistent with previous measurements [20]. Unentangled and entangled hydrogels also exhibit similar G'' behavior in this high-frequency regime, suggesting that association–dissociation dynamics of coiled-coil domains dominate the dissipative behavior at short times when entanglements have a minor role [37].

B. Rate-dependent deformation of protein-based physical gels

Unentangled and entangled associative protein hydrogels exhibited rate-dependent responses to uniaxial extension, as shown in engineering stress–strain curves taken during *in situ* SAXS and POM experiments (FIG. 6). The rate-dependent deformation of associative hydrogels is characterized using a dimensionless strain rate $\dot{\varepsilon}\tau$, where $\dot{\varepsilon}$ is the engineering strain rate and τ is a characteristic relaxation time. Unentangled and entangled gel deformation was normalized to the same associative coiled-coil relaxation time, which was identified by the maximum in G'' near $\omega_{\text{crossover}}$ such that $\tau = \omega_{\text{crossover}}^{-1} = 2.9$ seconds. Engineering strain rates of 0.028 and 0.084 s^{-1} corresponded to $\dot{\varepsilon}\tau = 0.08$ and 0.24 and are interchangeably referred to as 'slower' and 'faster' deformations, respectively. The dimensionless strain rate is analogous to the Weissenberg number Wi, which is typically based on the longest relaxation time of a polymer molecule τ_R and reserved for cases of steady flows [69]. Assigning a dimensionless strain rate based on the

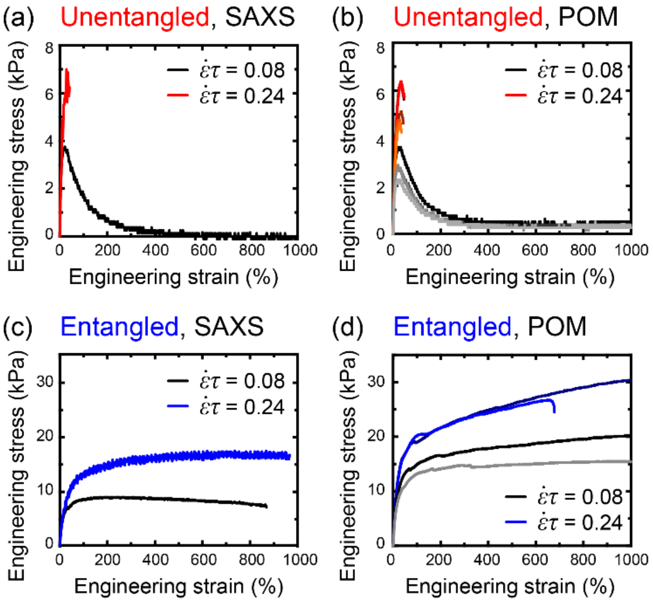

FIG. 6. Engineering stress–strain curves reveal rate-dependent response during uniaxial extensional deformation with *in situ* (a,c) SAXS and (b,d) POM on (a,b) unentangled and (c,d) entangled associative protein hydrogels. Individual curves are shaded for clarity.

junction relaxation time allowed a comparison between materials with different longest relaxation times: for a given engineering strain rate, the deformation of entangled physical gels (larger τ_R) proceeds at a larger Wi when compared to that of unentangled physical gels.

Unentangled hydrogels exhibited strongly rate-dependent tensile responses, as shown in FIG. 6a-b. During slower extensions, unentangled hydrogels were highly extensible, but during faster extensions, unentangled hydrogels underwent brittle failure at extensions of 39 ± 2%. At $\dot{\varepsilon}\tau = 0.08$, vertically loaded samples from *in situ* SAXS extended to the maximum range of the tensile stage (2,000% engineering strain), and horizontally loaded samples from *in situ* POM extended to at least 500% engineering strain before relaxing onto the testing apparatus. In both configurations, unentangled hydrogels briefly supported stress, followed by continuous stress relaxation associated with necking and sagging of the material during the deformation. The rate-dependent ductile and brittle behaviors of unentangled hydrogels are consistent with rupture modes observed in transient polymer networks, namely liquid-like thinning and solid-like fracture [88-90]. The transition between modes typically occurs near a critical Weissenberg number $Wi_c \approx 0.5$ [89], which exceeds the dimensionless strain rates ($0.08 < \dot{\varepsilon}\tau < 0.24$) and suggests a critical relaxation time that is longer than the junction relaxation time of 2.9 s.

Entangled hydrogels exhibited high toughness and extensibility in response to tensile deformation at both deformation rates (FIG. 6c-d). Entangled hydrogels supported stress throughout the extension, resulting in enhanced toughness (190,000 ± 45,000 and 210,000 ± 42,000 J/m^3 for $\dot{\varepsilon}\tau = 0.08$ and 0.24, respectively) relative to unentangled hydrogels (5,500 ± 500 and 1,700 ± 200 J/m^3 for $\dot{\varepsilon}\tau = 0.08$ and 0.24, respectively). High sample-to-sample variability is common in the mechanical testing of elastic gels [91]. Entangled physical gels exhibited rate-dependent stress plateaus, which are a signature of tough hydrogels with reversible crosslinks

[5,15,57]. However, entangled gels did not exhibit a ductile-to-brittle transition or the distinct failure modes observed in unentangled gels. During slower extensions, entangled hydrogel samples either stretched to the maximum range of the tensile stage (>2,000% engineering strain) or slipped from the testing apparatus (data not shown). During faster extensions, entangled hydrogel samples reached 1,040 ± 120% engineering strain before fracture.

C. Anisotropic nanostructure formation in entangled physical gels

In situ scattering experiments revealed that topological entanglements produce anisotropic nanostructural features during uniaxial extension. *In situ* SAXS was selected to investigate structural features from 1 – 100 nm with appropriate temporal resolution [40,55-58,70-77]. The orientation of associative network junctions was evaluated using the angular dependence of X-ray scattering profiles, from which azimuthal scattered intensity profiles were averaged over an annular ring at $q = 0.8 \pm 0.05$ nm^{-1} (FIG. 7). This q-range corresponds to features between 7.4 and 8.4 nm, which is slightly larger than a single coiled-coil bundle (7.3 nm in length).

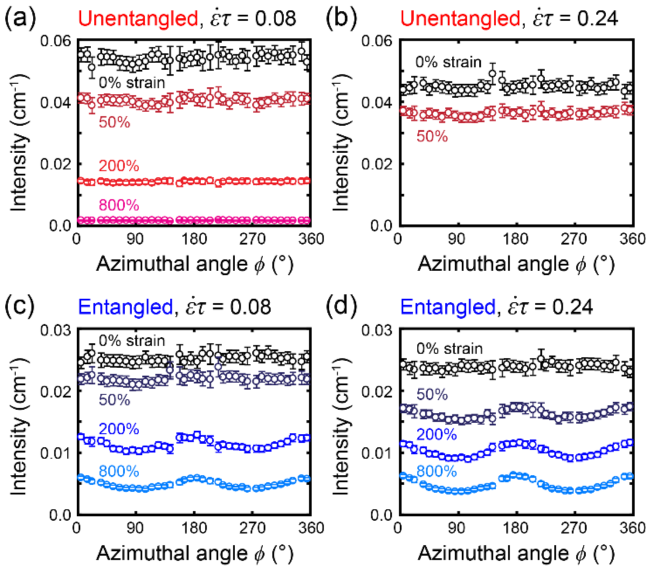

FIG. 7. Azimuthal angle dependence of scattered intensity at 0%, 50%, 200%, and 800% engineering strain reveals the evolution of (a,b) rate-independent, isotropic scattering from unentangled associative hydrogels and (c,d) rate-dependent anisotropic scattering from entangled associative hydrogels.

Isotropic scattering from unentangled protein hydrogels suggests rapid, molecular-scale stress relaxation mechanisms during extension. The scattered intensity at $q = 0.8 \pm 0.05$ nm^{-1} was independent of azimuthal angle □ (□ = 0° corresponds to scattering perpendicular to strain) at both deformation rates and at all elongations, suggesting that coiled-coil groups recover random orientations throughout the material during the entire deformation. Rapid rearrangement of network junctions during extension is consistent with liquid-like thinning and solid-like fracture mechanisms observed at $\dot{\varepsilon}\tau = 0.08$ and 0.24, respectively [88-90].

In entangled physical gels, the emergence of anisotropic nanostructure increased the scattering signal perpendicular to the straining axis, which is visible as peaks near □ = 0° and 180°. Anisotropy in the scattered intensity was evident at smaller engineering strains under faster deformation, suggesting an earlier onset of molecular alignment and orientation due to unrelaxed network junctions. Similar rate-dependent structural responses observed during *in situ* SAXS of supramolecular hydrogels illustrate the need to consider both strain rate and relaxation times in the design of tough and extensible soft materials [57]. In all samples, the scattered intensity at $q = 0.8 \pm 0.05$ nm^{-1} and at all azimuthal angles decreased as the deformation proceeded due to thinning of the hydrogel materials.

Hermans' orientation factor f_{H} enables quantification of domain alignment and orientation in associative protein gels and comparison to other anisotropic materials (FIG. 8) [92,93]:

$$f_{\mathrm{H}} = \frac{3\langle \cos^2 \phi \rangle - 1}{2} \tag{3}$$

$$\langle cos^2\, \phi \rangle = \frac{\int_{\pi/2}^{\pi} I(\phi) \cos^2 \phi \sin \phi \, \mathrm{d}\phi}{\int_{\pi/2}^{\pi} I(\phi) \sin \phi \, \mathrm{d}\phi} \tag{4}$$

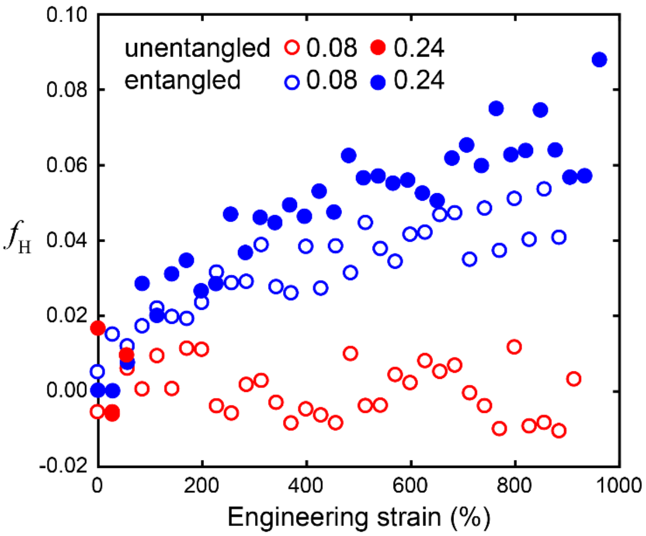

FIG. 8. Hermans' orientation factor during tensile deformation at $\dot{\varepsilon}\tau = 0.08$ (◦) and 0.24 (•) suggests isotropic molecular configurations throughout the tensile deformation of unentangled (red) associative hydrogels. In contrast, entangled (blue) hydrogels undergo weak nanostructural alignment in the direction parallel to the straining axis.

where $f_{\mathrm{H}} = 1$ indicates c $= 0$ indicates an isotropic material, and $f_{\mathrm{H}} = -½$ indicates alignment perpendicular to the straining axis. For unentangled hydrogels, $f_{\mathrm{H}} = 0$ at all strains, consistent with isotropic materials. Entangled hydrogels exhibited rate-dependent anisotropy and alignment. At both deformation rates, f_{H} increased with respect to engineering strain, reaching maximum values of $f_{\mathrm{H}} = 0.05$ at $\dot{\varepsilon}\tau = 0.08$ and $f_{\mathrm{H}} = 0.09$ at $\dot{\varepsilon}\tau = 0.24$. The relatively small values of f_{H} are consistent with an amorphous polymeric material with weak alignment of nanostructural domains parallel to the straining axis [94-96].

Specific anisotropic features of entangled physical gels were identified from 1D radial scattering profiles (FIG. 9). Radial scattering profiles were generated from 2D scattering patterns by averaging sectors centered on the axes parallel and perpendicular to strain. Radial profiles were analyzed in the context of the broad peak model (Eq. 2), from which the peak position q_0 and correlation length ξ quantify nanostructural features of associative protein gels [56,57,79,80].

Unentangled hydrogels exhibited isotropic scattering throughout tensile deformation (FIG. 9a-b), which was reflected by similar values of q_0 and ξ in the parallel and perpendicular directions (FIG. 10). During a slower extension, unentangled hydrogels exhibited nearly constant peak positions of 0.55 ± 0.01 nm^{-1} and correlation lengths of 2.4 ± 0.1 nm up to 500% strain (FIG. 10a,c). Beyond 500% engineering strain, large fluctuations in $q_{0,\parallel}$ and $q_{0,\perp}$ are attributed to decreased scattered intensity from sample thinning and the onset of sample failure.

The isotropic, near-constant nanostructures during deformation of unentangled gels suggest that unentangled associative protein molecules do not undergo local stretching. Instead, physical crosslinking junctions undergo dissociation–association dynamics to allow the rapid rearrangement of molecules in the gel. This relaxation mechanism is hypothesized to permit high

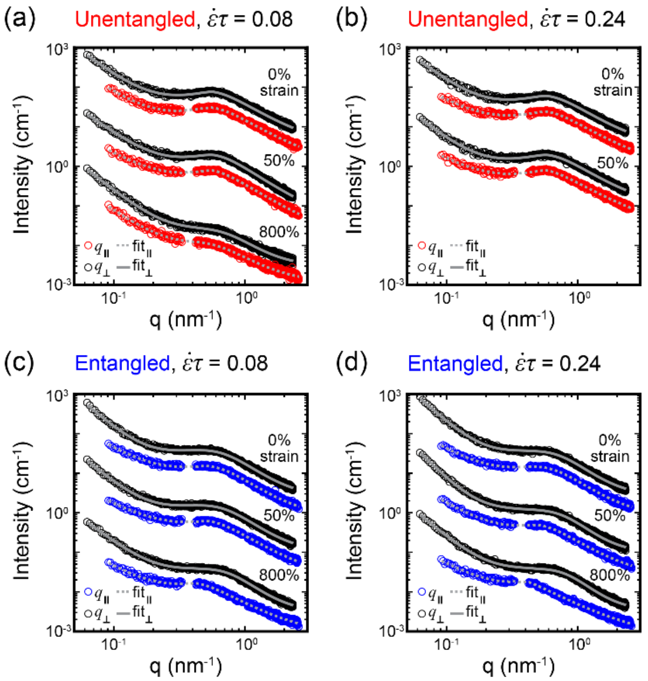

FIG. 9. 1D radial scattering profiles from (a,b) unentangled and (c,d) entangled associative protein hydrogels reveal anisotropic changes in scattered intensity during deformation. 1D scattering in the directions perpendicular (black) and parallel (red and blue) to the straining axis are shown for the start of uniaxial extension, 50% engineering strain, and 800% engineering strain. Lines indicate fits to the broad peak model, and data are offset vertically for

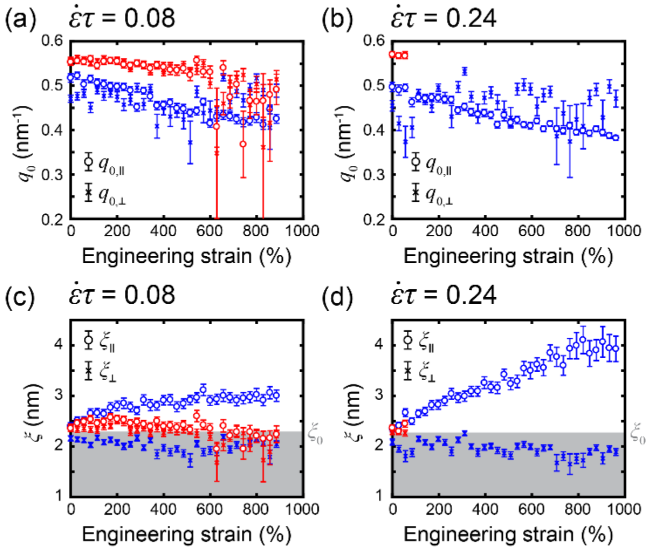

FIG. 10. Broad peak scattering model parameters (a,b) q_0 and (c,d) ξ suggest rate-dependent, anisotropic changes to the nanostructure of entangled associative hydrogels during tensile deformation (blue). In contrast, unentangled hydrogels remain isotropic (red). Error bars represent 95% confidence intervals. The gray region indicates correlation lengths that are smaller than the quiescent ξ_0 = 2.3 nm.

extensibility when the rate of deformation is slower than the rate of junction rearrangement, as illustrated in FIG. 11a. During a faster extension, q_0 and ξ do not undergo significant changes in unentangled gels (FIG. 10b,d) in the limited deformation before failure, suggesting that brittle failure results from the reduced ability of network junctions to rearrange or relax during rapid deformations.

Conversely, radial scattering profiles of entangled hydrogels reveal the emergence of several anisotropic features at both strain rates, including an increase in the overall scattered intensity in the direction perpendicular to strain when compared to the direction parallel to strain (FIG. 9c-d). Table I summarizes changes in each direction for scattering peak positions q_0 and correlation lengths ξ during deformation. In the strain direction, the scattering peak position visibly shifted to lower q values with increasing engineering strain. This trend is quantified by significant, monotonic decreases in the fit parameter $q_{0,\parallel}$ (FIG. 10a-b). Decreases in $q_{0,\parallel}$ were accompanied by strain-rate dependent increases in $\xi_\parallel$ and decreases in $\xi_\perp$ (FIG. 10c-d).

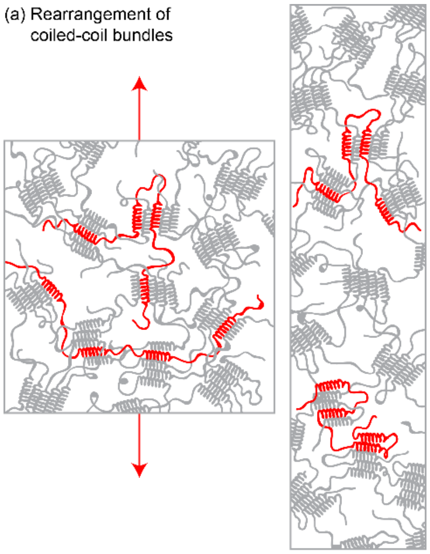

(a) Rearrangement of coiled-coil bundles

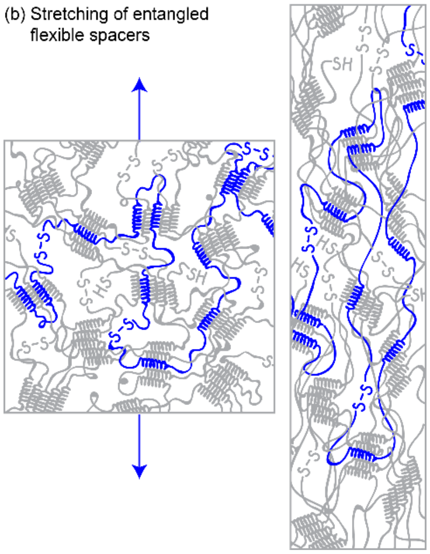

(b) Stretching of entangled flexible spacers

FIG. 11. Molecular mechanisms in associative protein gels. (a) Associative group rearrangement leads to high extensibility, and (b) entanglements support stress and chain stretching to enable high toughness.

TABLE I. Broad peak model fit parameters from 1D profiles of entangled associative hydrogels; errors represent 95% confidence intervals.

$\dot{\varepsilon}\tau$	Strain	$q_{0,\parallel}$ (nm^{-1})	$q_{0,\perp}$ (nm^{-1})	$\xi_{\parallel}$ (nm)	$\xi_{\perp}$ (nm)
0.08	0 %	0.52 ± 0.01	0.47 ± 0.01	2.4 ± 0.1	2.2 ± 0.1
0.08	800 %	0.43 ± 0.01	0.52 ± 0.01	3.0 ± 0.1	2.2 ± 0.1
0.24	0 %	0.50 ± 0.01	0.45 ± 0.01	2.4 ± 0.1	2.1 ± 0.1
0.24	800 %	0.39 ± 0.01	0.42 ± 0.03	4.0 ± 0.3	1.8 ± 0.1

The collective changes in q_0 and ξ in the entangled gels suggest an increase in the center-of-mass spacing of network junctions in the straining direction. Assuming that the rigid secondary structure of coiled-coil bundles prevents internal stretching of network junctions, two distinct molecular mechanisms may contribute to the increased spacing of junctions in an entangled physical gel. First, bundle rotation and aligned orientation in the straining direction would lead to the development of elongated asymmetric domains. Second, flexible spacer stretching would allow for changes in the spatial distribution of junctions with isotropic orientations.

In the case of bundle rotation without spacer stretching, the domain spacing in the straining direction should reach a maximum at the axial spatial extent of a pentameric bundle flanked by C_{10} spacers (13.1 nm or $q_{0,\parallel} = 0.48$ nm^{-1}). This hypothetical maximum spacing is smaller than the final measured *d*-spacings of 14.6 ± 0.4 nm and 16.5 ± 0.4 nm ($\dot{\varepsilon}\tau = 0.08$ and 0.24, respectively), suggesting substantial contributions from other mechanisms. Rotation of associative bundles without chain stretching would also lead to a decrease in the domain spacing perpendicular to strain to the radial spatial extent of the bundle (8.8 nm or $q_{0,\perp} = 0.71$ nm^{-1}). In contrast, the peak position $q_{0,\perp}$ only increased slightly when $\dot{\varepsilon}\tau = 0.08$, likely due to conservation of volume during hydrogel elongation. At $\dot{\varepsilon}\tau = 0.24$, $q_{0,\perp}$ fluctuated around a nearly constant average of 13.7 ± 1.2 nm ($q_{0,\perp} = 0.46 \pm 0.4$ nm^{-1}, FIG. 10b). Notably, $\xi_\perp$ did not change significantly at either strain rate. Insignificant changes in $q_{0,\perp}$ and $\xi_\perp$ may result from the inability of junctions to relax during deformation. These results support stretching of flexible C_{10} spacers as a major mechanism of increased domain spacing within entangled hydrogels.

Toughness results from integrating energy dissipation mechanisms into a network that maintains elasticity [5,22,23]. Topological entanglements form a secondary elastic network in chain-extended associative protein gels, and stress relaxation mechanisms include both stretching of flexible spacers and rearrangement of network junctions (FIG. 11b). In the absence of molecular rearrangement, changes in $\xi_{\parallel}$ would be independent of the deformation rate. Instead, $\xi_{\parallel}$ was smaller during a slow deformation than during a fast deformation at equivalent engineering strains (FIG. 10c-d). Network junction rearrangement is also consistent with the observation that entangled associative protein hydrogels stretched to the maximum range of the tensile stage during slow deformations ($\dot{\varepsilon}\tau = 0.08$, >2,000% strain), whereas samples failed at 1,040 ± 120% engineering strain during fast deformations ($\dot{\varepsilon}\tau = 0.24$). Entangled physical gel failure under faster deformation is attributed to the inability of network junctions to relax during deformation; this molecular mechanism resembles that of brittle failure in the rapid deformation of unentangled physical gels.

D. Macroscopic alignment of entangled physical gels

In situ POM experiments revealed enhanced birefringence of entangled physical gels in comparison to unentangled gels (FIG. 12), suggesting a strong effect of topological entanglement

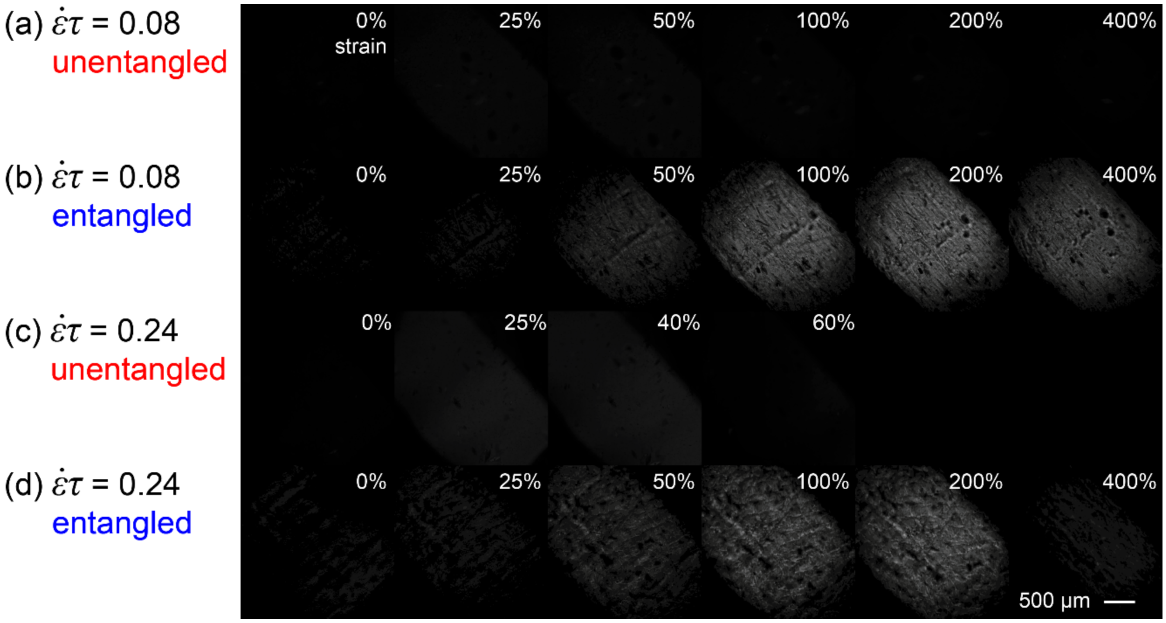

FIG. 12. Time-lapse images from *in situ* POM reveal macroscopic responses during uniaxial extension of (a,c) unentangled and (b,d) entangled associative protein hydrogels. Intensities are normalized to account for a neutral-density filter used during entangled hydrogel tests. Videos corresponding to each image series are included in the Supplemental Material [68].

on macroscopic alignment. Birefringence from unentangled gels corresponded directly to the stress response (FIG. 6b, FIG. 13a), indicating macroscopic alignment in the direction of loading [97]. At both deformation rates, initial increases in birefringence matched initial increases in stress, as expected for small deformations governed by linear stress-optical relationships [64-67,69]. During slow deformations, unentangled hydrogels exhibited a maximum birefringent intensity I_{PF} of 5 ± 1% near 30% engineering strain, followed by a decay corresponding to high extensibility of the gel. Decaying birefringence is consistent with stress relaxation due to the rearrangement of unentangled associative protein molecules [67]. The unentangled material was not birefringent at larger extensions (> 200% engineering strain), which is attributed to the recovery of an isotropic structure within the imaging region. This structural recovery corresponds to the liquid-like thinning behavior and isotropic nanostructures observed by *in situ* SAXS during the slow elongation of unentangled hydrogels. Faster deformation of unentangled

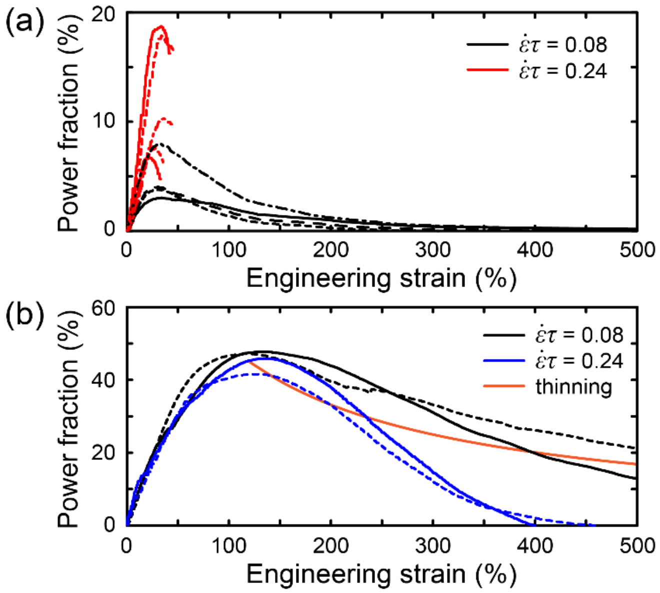

FIG. 13. Non-monotonic birefringent signals emerge during *in situ* POM of (a) unentangled and (b) entangled associative protein hydrogels during extensional deformation. Solid and dashed lines indicate distinct samples. The orange line in (b) indicates the decrease in birefringence due to sample thinning only. Enhanced birefringence of entangled hydrogels relative to unentangled hydrogels suggests that entanglements allow the alignment and orientation of protein

hydrogels resulted in I_{PF} increasing to 12 ± 3% prior to brittle failure at 39 ± 2% engineering strain. The deformation rate exceeded the rate of stress dissipation, and the birefringent intensity reached a plateau prior to sample fracture. This result suggests that molecular-scale relaxation and stress dissipation were unable to occur, which is consistent with the hypothesis that molecular relaxation and junction rearrangement mechanisms enable the high extensibility of associative hydrogels (FIG. 11a).

Entangled physical gels exhibited rate-dependent, nonmonotonic birefringence (FIG. 13b), in contrast to monotonic birefringence typically observed in tough, chemically crosslinked gels with fixed network junctions [64-66]. Nonmonotonic birefringence requires structural rearrangement during uniaxial extension and rarely emerges from stretched polymer networks, with notable exceptions including composite polymer–nanoparticle gels [62,63] and double-network hydrogels comprising both physical and chemical crosslinks [59]. In entangled associative protein gels, I_{PF} increased to a peak value before a slow, continuous decay. The birefringence peak was similar at both strain rates, but rate-dependent signal decays suggest different stress relaxation mechanisms. At $\dot{\varepsilon}\tau = 0.08$, the birefringent intensity did not decay to zero during the period of video acquisition, whereas at $\dot{\varepsilon}\tau = 0.24$, the intensity decayed to zero at an average engineering strain of 430 ± 30%. Nonmonotonicity was not observed in the stress response, where gels stretched elastically up to 20% strain, followed by a transition to a stress plateau corresponding with plastic deformation at both deformation rates (FIG. 6c-d).

The nonmonotonic birefringent response of entangled physical gels during *in situ* POM suggests an interplay between multiple mechanisms to produce high extensibility and toughness. The initial increase in birefringent intensity spanned both the region of elastic deformation and the transition to plastic deformation, suggesting that the elongation of flexible spacer domains allows bulk alignment within stretched hydrogels (FIG. 11b). Order-of-magnitude increases in birefringent signals from entangled gels compared to unentangled gels further support the proposed mechanisms of domain stretching in entangled gels and rapid molecular relaxation in unentangled gels. After entangled hydrogels yielded and entered the region of plastic deformation, strain-rate dependent decays in birefringent intensity were observed. Decreasing birefringent intensity is considered to emerge from two primary effects: (1) thinning of hydrogel samples as the stretching deformation proceeds, and (2) force-activated relaxation of associative protein molecules.

Sample thinning is considered to produce a proportional decrease in birefringent intensity with respect to sample thickness, or path length, as estimated by the orange line in FIG. 13b. This estimation assumed that the birefringent power fraction is proportional to the path length for polymeric samples containing randomly oriented, optically anisotropic grains [97-99], changes in the average grain size are negligible compared to changes in the sample thickness, and the hydrogel maintains constant concentration during elongation. The path length (sample thickness) was calculated assuming that hydrogel deformation follows the linear elastic behavior of a material with Poisson's ratio $\nu = 0.5$, which is typical for polymer networks and swollen hydrogels [100,101]. Path length calculations accounted for hydrogels with initial dimensions of 3.5 mm tall, 4.0 mm wide, and 2.0 mm thick, based on the initial clamp displacement L_0 and sample mold dimensions. The initial I_{PF} was based on the average maximum value for entangled hydrogels (45% at 120% engineering strain). Initially, the birefringence of entangled associative hydrogels overshot the estimated intensity, which is attributed to the dynamic formation of aligned structures during hydrogel stretching. As the deformation proceeded at $\dot{\varepsilon}\tau = 0.08$, I_{PF} followed the sample thinning prediction. Sustained birefringence during a slower deformation suggests that network junction rearrangement prevents the rupture of flexible spacer domains, such that entangled chains are able to stretch and orient along the straining axis to produce macroscopically aligned structures. The mechanisms of junction rearrangement and spacer stretching are consistent with the sustained nanoscale anisotropy observed during *in situ* SAXS experiments, as well as the macroscopic properties of high extensibility and toughness.

During the deformation at $\dot{\varepsilon}\tau = 0.24$, entangled gels supported larger stress loads (FIG. 6c,d) and rapid birefringence decays (FIG. 13b, blue curves) that suggest stress dissipation by force-activated relaxation mechanisms [102,103]. Force-activated relaxation arises from the inability of polymer molecules to sustain high stretch at large strain rates, which is frequently observed as material failure during uniaxial extensional strain [104-106]. Force-activated relaxation mechanisms are further supported by the fracture of entangled hydrogels at 1,040 ± 120% strain while stretching at $\dot{\varepsilon}\tau = 0.24$, whereas samples stretched at $\dot{\varepsilon}\tau = 0.08$ extended to the maximum range of the tensile stage (>2,000% strain). Potential molecular-scale relaxation mechanisms include the release of topological entanglements, rearrangement of associative domains, and/or backbone chain scission. Although disulfide bridges have lower bond energies than protein backbone bonds and are known to rearrange as mechanically labile bonds [107-109], coiled-coil associations have significantly lower bond energies and are more likely to rearrange first. Nonmonotonic birefringence is consistent with *in situ* SAXS observations, where a faster deformation produced a larger average distance between associative domains. This increased spacing likely results from a combination of flexible spacer stretching and breakage of physical and/or chemical bonds. The potential shortening of protein chains and release of topological entanglements are both consistent with the materials' reduced ability to sustain macroscopically aligned structures.

IV. CONCLUSIONS

The contribution of topological entanglement to the tensile response—in particular, toughness and extensibility—of physical gels was determined using *in situ* SAXS and POM of well-defined associative protein hydrogels. Artificially engineered proteins were selected as an ideal model system for investigating the function of entanglements. Here, the protein molecular weight was increased beyond the entanglement cutoff by oxidative chain extension [20,39]. Unentangled and chain-extended protein gels shared quiescent nanostructural features, but the linear viscoelastic response revealed topological entanglements in chain-extended hydrogels.

Rheo-optical signatures from unentangled physical gels suggest rapid relaxation mechanisms at the nanoscale, such that network junctions freely rearrange during deformation. During uniaxial tensile testing, unentangled gels exhibited strongly rate-dependent stress responses. Unentangled gels underwent a ductile-to-brittle transition with increasing extensional strain rate, with failure modes resembling those of liquid-like thinning and solid-like fracture of transient polymer networks [88-90]. This transition was coupled with rate-independent isotropic X-ray scattering and weak, rapidly decaying birefringence during uniaxial extension.

In contrast, topological entanglement produced a two-order-of-magnitude enhancement in toughness of chain-extended gels when compared to unentangled gels. In entangled physical gels, local stress dissipation mechanisms enable improved toughness and high extensibility. Entangled hydrogels developed anisotropic X-ray scattering and strong, non-monotonic birefringence in response to uniaxial strain, suggesting that entanglements allow a high degree of chain stretching and alignment to support stress. The eventual decay of birefringence during the extension of entangled hydrogels suggests that high extensibility emerges from rearrangement of coiled-coil associative domains and local stress dissipation.

Model associative protein hydrogels enabled the identification of molecular-scale mechanisms that give rise to high toughness and extensibility of entangled physical networks. Critical insight into these phenomena has the potential to advance the design and synthesis of tough and extensible polymer networks with diverse chemistries, enabling the broad development of mechanically robust, self-healing, and functional soft materials.

ACKNOWLEDGMENTS

This work was supported by the National Science Foundation (DMR-1709315) and the U.S. Army Research Office through the Institute of Soldier Nanotechnologies under Contract W911NF-07-D-0004. DJM acknowledges support by the Arnold and Mabel Beckman Foundation. We thank Eric Schaible at Lawrence Berkeley National Laboratory for assistance with SAXS experiments. We also thank M. K. Sing, R. K. Avery, and B. M. Seifried for helpful discussions, as well as all members of the Olsen research group. This research used resources of the Advanced Light Source, which is a DOE Office of Science User Facility under contract no. DE-AC02-05CH11231.

REFERENCES

[1] Functional Supramolecular Polymers. T. Aida, E. W. Meijer, and S. I. Stupp, Science **335**, 813 (2012).

[2] Supramolecular polymeric hydrogels. E. A. Appel, J. del Barrio, X. J. Loh, and O. A. Scherman, Chemical Society Reviews **41**, 6195 (2012).

[3] Adaptable Hydrogel Networks with Reversible Linkages for Tissue Engineering. W. Huiyuan and H. S. C., Advanced Materials **27**, 3717 (2015).

[4] The design of reversible hydrogels to capture extracellular matrix dynamics. A. M. Rosales and K. S. Anseth, Nature Reviews Materials **1**, 15012 (2016).

[5] Multi-scale multi-mechanism design of tough hydrogels: building dissipation into stretchy networks. X. Zhao, Soft Matter **10**, 672 (2014).

[6] Tuning the erosion rate of artificial protein hydrogels through control of network topology. W. Shen, K. Zhang, J. A. Kornfield, and D. A. Tirrell, Nature Materials **5**, 153 (2006).

[7] Yielding Behavior in Injectable Hydrogels from Telechelic Proteins. B. D. Olsen, J. A. Kornfield, and D. A. Tirrell, Macromolecules **43**, 9094 (2010).

[8] Assembly of an Artificial Protein Hydrogel through Leucine Zipper Aggregation and Disulfide Bond Formation. W. Shen, R. G. H. Lammertink, J. K. Sakata, J. A. Kornfield, and D. A. Tirrell, Macromolecules **38**, 3909 (2005).

[9] Reversible Hydrogels from Self-Assembling Artificial Proteins. W. A. Petka, J. L. Harden, K. P. McGrath, D. Wirtz, and D. A. Tirrell, Science **281**, 389 (1998).

[10] Intrinsically stretchable and healable semiconducting polymer for organic transistors. J. Y. Oh, S. Rondeau-Gagné, Y.-C. Chiu, A. Chortos, F. Lissel, G.-J. N. Wang, B. C. Schroeder, T. Kurosawa, J. Lopez, T. Katsumata, J. Xu, C. Zhu, X. Gu, W.-G. Bae, Y. Kim, L. Jin, J. W. Chung, J. B. H. Tok, and Z. Bao, Nature **539**, 411 (2016).

[11] A Transparent, Self-Healing, Highly Stretchable Ionic Conductor. Y. Cao, T. G. Morrissey, E. Acome, S. I. Allec, B. M. Wong, C. Keplinger, and C. Wang, Advanced Materials **29**, 1605099 (2017).

[12] A highly stretchable autonomous self-healing elastomer. C.-H. Li, C. Wang, C. Keplinger, J.-L. Zuo, L. Jin, Y. Sun, P. Zheng, Y. Cao, F. Lissel, C. Linder, X.-Z. You, and Z. Bao, Nature Chemistry **8**, 618 (2016).

[13] pH-induced metal-ligand cross-links inspired by mussel yield self-healing polymer networks with near-covalent elastic moduli. N. Holten-Andersen, M. J. Harrington, H. Birkedal, B. P. Lee, P. B. Messersmith, K. Y. C. Lee, and J. H. Waite, Proceedings of the National Academy of Sciences **108**, 2651 (2011).

[14] Tuning Dynamic Mechanical Response in Metallopolymer Networks through Simultaneous Control of Structural and Temporal Properties of the Networks. D. Mozhdehi, J. A. Neal, S. C. Grindy, Y. Cordeau, S. Ayala, N. Holten-Andersen, and Z. Guan, Macromolecules **49**, 6310 (2016).

[15] Stimuli-Responsive Supramolecular Hydrogels with High Extensibility and Fast Self-Healing via Precoordinated Mussel-Inspired Chemistry. S. Hou and P. X. Ma, Chemistry of Materials **27**, 7627 (2015).

[16] A Facile Way to Tune Mechanical Properties of Artificial Elastomeric Proteins-Based Hydrogels. J. Fang and H. Li, Langmuir **28**, 8260 (2012).

[17] Superstretchable, Self-Healing Polymeric Elastomers with Tunable Properties. P.-F. Cao, B. Li, T. Hong, J. Townsend, Z. Qiang, K. Xing, K. D. Vogiatzis, Y. Wang, J. W. Mays, A. P. Sokolov, and T. Saito, Advanced Functional Materials **28**, 1800741 (2018).

[18] Tough Supramolecular Polymer Networks with Extreme Stretchability and Fast Room-Temperature Self-Healing. J. Liu, C. S. Y. Tan, Z. Yu, N. Li, C. Abell, and O. A. Scherman, Advanced Materials **29**, 1605325 (2017).

[19] Toughening of Thermoresponsive Arrested Networks of Elastin-Like Polypeptides To Engineer Cytocompatible Tissue Scaffolds. M. J. Glassman, R. K. Avery, A. Khademhosseini, and B. D. Olsen, Biomacromolecules **17**, 415 (2016).

[20] Oxidatively Responsive Chain Extension to Entangle Engineered Protein Hydrogels. S. Tang, M. J. Glassman, S. Li, S. Socrate, and B. D. Olsen, Macromolecules **47**, 791 (2014).

[21] An injectable shear-thinning biomaterial for endovascular embolization. R. K. Avery, H. Albadawi, M. Akbari, Y. S. Zhang, M. J. Duggan, D. V. Sahani, B. D. Olsen, A. Khademhosseini, and R. Oklu, Science Translational Medicine **8**, 365ra156 (2016).

[22] Why are double network hydrogels so tough? J. P. Gong, Soft Matter **6**, 2583 (2010).

[23] A review on tough and sticky hydrogels. C. W. Peak, J. J. Wilker, and G. Schmidt, Colloid and Polymer Science **291**, 2031 (2013).

[24] Protein-based materials, toward a new level of structural control. J. C. M. van Hest and D. A. Tirrell, Chemical Communications, 1897 (2001).

[25] Artificially Engineered Protein Polymers. Y. J. Yang, A. L. Holmberg, and B. D. Olsen, Annual Review of Chemical and Biomolecular Engineering **8**, 549 (2017).

[26] Peptide-based stimuli-responsive biomaterials. R. J. Mart, R. D. Osborne, M. M. Stevens, and R. V. Ulijn, Soft Matter **2**, 822 (2006).

[27] Smart Hydrogels Containing Adenylate Kinase: Translating Substrate Recognition into Macroscopic Motion. W. Yuan, J. Yang, P. Kopečková, and J. Kopeček, Journal of the American Chemical Society **130**, 15760 (2008).

[28] Fibronectin extension and unfolding within cell matrix fibrils controlled by cytoskeletal tension. G. Baneyx, L. Baugh, and V. Vogel, Proceedings of the National Academy of Sciences **99**, 5139 (2002).

[29] Dynamic Presentation of Immobilized Ligands Regulated through Biomolecular Recognition. B. Liu, Y. Liu, J. J. Riesberg, and W. Shen, Journal of the American Chemical Society **132**, 13630 (2010).

[30] Phase transition-induced elasticity of α-helical bioelastomeric fibres and networks. A. Miserez and P. A. Guerette, Chemical Society Reviews **42**, 1973 (2013).

[31] Peptide Hydrogels – Versatile Matrices for 3D Cell Culture in Cancer Medicine. P. Worthington, D. J. Pochan, and S. A. Langhans, Frontiers in Oncology **5** (2015).

[32] β-hairpin peptide hydrogels for package delivery. P. Worthington, S. Langhans, and D. Pochan, Advanced Drug Delivery Reviews **110-111**, 127 (2017).

[33] Hybrid hydrogels assembled from synthetic polymers and coiled-coil protein domains. C. Wang, R. J. Stewart, and J. Kopeček, Nature **397**, 417 (1999).

[34] Reversible Hydrogels from Self-Assembling Genetically Engineered Protein Block Copolymers. C. Xu, V. Breedveld, and J. Kopeček, Biomacromolecules **6**, 1739 (2005).

[35] Structure and mechanical response of protein hydrogels reinforced by block copolymer self-assembly. M. J. Glassman and B. D. Olsen, Soft Matter **9**, 6814 (2013).

[36] Reinforcement of Shear Thinning Protein Hydrogels by Responsive Block Copolymer Self-Assembly. M. J. Glassman, J. Chan, and B. D. Olsen, Advanced Functional Materials **23**, 1182 (2013).

[37] Anomalous Self-Diffusion and Sticky Rouse Dynamics in Associative Protein Hydrogels. S. Tang, M. Wang, and B. D. Olsen, Journal of the American Chemical Society **137**, 3946 (2015).

[38] Controlled Structure in Artificial Protein Hydrogels. S. B. Kennedy, K. Littrell, P. Thiyagarajan, D. A. Tirrell, and T. P. Russell, Macromolecules **38**, 7470 (2005).

[39] Controlling topological entanglement in engineered protein hydrogels with a variety of thiol coupling chemistries. S. Tang and B. D. Olsen, Frontiers in Chemistry **2** (2014).

[40] Structure and rheology of dual-associative protein hydrogels under nonlinear shear flow. M. K. Sing, M. J. Glassman, X. T. Vronay-Ruggles, W. R. Burghardt, and B. D. Olsen, Soft Matter **13**, 8511 (2017).

[41] Genetic Synthesis of Periodic Protein Materials. M. J. Fournier, H. S. Creel, K. P. McGrath, M. T. Krejchi, E. D. T. Atkins, T. L. Mason, and D. A. Tirrell, Journal of Bioactive and Compatible Polymers **6**, 326 (1991).

[42] Genetically directed syntheses of new polymeric materials. Expression of artificial genes encoding proteins with repeating -(AlaGly)3ProGluGly- elements. K. P. McGrath, M. J. Fournier, T. L. Mason, and D. A. Tirrell, Journal of the American Chemical Society **114**, 727 (1992).

[43] Influence of proline residues on protein conformation. M. W. MacArthur and J. M. Thornton, Journal of Molecular Biology **218**, 397 (1991).

[44] The Role of Proline and Glycine in Determining the Backbone Flexibility of a Channel-Forming Peptide. J. Jacob, H. Duclohier, and D. S. Cafiso, Biophysical Journal **76**, 1367 (1999).

[45] Glycine Residues Provide Flexibility for Enzyme Active Sites. B. X. Yan and Y. Q. Sun, Journal of Biological Chemistry **272**, 3190 (1997).

[46] Coiled coils: new structures and new functions. A. Lupas, Trends in Biochemical Sciences **21**, 375 (1996).

[47] Coiled Coil Domains: Stability, Specificity, and Biological Implications. J. M. Mason and K. M. Arndt, ChemBioChem **5**, 170 (2004).

[48] Self-assembly and soluble aggregate behavior of computationally designed coiled-coil peptide bundles. M. J. Haider, H. V. Zhang, N. Sinha, J. A. Fagan, K. L. Kiick, J. G. Saven, and D. J. Pochan, Soft Matter **14**, 5488 (2018).

[49] A thermodynamic scale for leucine zipper stability and dimerization specificity: e and g interhelical interactions. D. Krylov, I. Mikhailenko, and C. Vinson, The EMBO Journal **13**, 2849 (1994).

[50] Thermodynamic Characterization of the Coupled Folding and Association of Heterodimeric Coiled Coils (Leucine Zippers). I. Jelesarov and H. R. Bosshard, Journal of Molecular Biology **263**, 344 (1996).

[51] N-Terminal Aliphatic Residues Dictate the Structure, Stability, Assembly, and Small Molecule Binding of the Coiled-Coil Region of Cartilage Oligomeric Matrix Protein. S. K. Gunasekar, M. Asnani, C. Limbad, J. S. Haghpanah, W. Hom, H. Barra, S. Nanda, M. Lu, and J. K. Montclare, Biochemistry **48**, 8559 (2009).

[52] Bond Energies in *Encyclopedia of Inorganic Chemistry*, edited by R. B. King, R. H. Crabtree, C. M. Lukehart, D. A. Atwood, and R. A. Scott (2006).

[53] Multifunctional, High Molecular Weight, Post-Translationally Modified Proteins through Oxidative Cysteine Coupling and Tyrosine Modification. B. M. Seifried, J. Cao, and B. D. Olsen, Bioconjugate Chemistry **29**, 1876 (2018).

[54] Deformation mechanism of nanocomposite gels studied by contrast variation small-angle neutron scattering. T. Nishida, H. Endo, N. Osaka, H.-j. Li, K. Haraguchi, and M. Shibayama, Physical Review E **80**, 030801 (2009).

[55] Molecular weight effects on tensile properties of blend hydrogels composed of clay and polymers. H. Takeno and Y. Kimura, Polymer **85**, 47 (2016).

[56] Nanostructure Evolution during Relaxation from a Large Step Strain in a Supramolecular Copolymer-Based Hydrogel: A SANS Investigation. C. G. Wiener, C. Wang, Y. Liu, R. A. Weiss, and B. D. Vogt, Macromolecules **50**, 1672 (2017).

[57] Strain rate dependent nanostructure of hydrogels with reversible hydrophobic associations during uniaxial extension. C. Wang, C. G. Wiener, M. Fukuto, R. Li, K. G. Yager, R. A. Weiss, and B. D. Vogt, Soft Matter (2019).

[58] Influence of End-Block Dynamics on Deformation Behavior of Thermoresponsive Elastin-like Polypeptide Hydrogels. M. K. Sing, W. R. Burghardt, and B. D. Olsen, Macromolecules **51**, 2951 (2018).

[59] Strain-Induced Molecular Reorientation and Birefringence Reversion of a Robust, Anisotropic Double-Network Hydrogel. Z. L. Wu, D. Sawada, T. Kurokawa, A. Kakugo, W. Yang, H. Furukawa, and J. P. Gong, Macromolecules **44**, 3542 (2011).

[60] Liquid crystalline inorganic nanosheets for facile synthesis of polymer hydrogels with anisotropies in structure, optical property, swelling/deswelling, and ion transport/fixation. N. Miyamoto, M. Shintate, S. Ikeda, Y. Hoshida, Y. Yamauchi, R. Motokawa, and M. Annaka, Chemical Communications **49**, 1082 (2013).

[61] Morphology of oriented calcium alginate gels obtained by the flow-gelation method. F. Yokoyama, E. C. Achife, M. Matsuoka, K. Shimamura, Y. Yamashita, and K. Monobe, Polymer **32**, 2911 (1991).

[62] Optical anisotropy in polymer–clay nanocomposite hydrogel and its change on uniaxial deformation. K. Murata and K. Haraguchi, Journal of Materials Chemistry **17**, 3385 (2007).

[63] Mechanical/optical behaviors of imogolite hydrogels depending on their compositions and oriented structures. K. Shikinaka, Y. Koizumi, and K. Shigehara, Journal of Applied Polymer Science **132** (2015).

[64] Mechano-optical behavior of loosely crosslinked double-network hydrogels: Modeling and real-time birefringence measurement during uniaxial extension. S. Shams Es-haghi, I. Offenbach, D. Debnath, R. A. Weiss, and M. Cakmak, Polymer **115**, 239 (2017).

[65] Mechanical and Optical Behavior of Double Network Rubbers. P. H. Mott and C. M. Roland, Macromolecules **33**, 4132 (2000).

[66] Experimental results relating stress and birefringence to strain in poly(dimethylsiloxane) networks. Comparisons with theory. B. Erman and P. J. Flory, Macromolecules **16**, 1607 (1983).

[67] Nonlinear Mechano-Optical Behavior and Strain-Induced Structural Changes of l-Valine-Based Poly(ester urea)s. K. Chen, N. Z. Dreger, F. Peng, B. D. Vogt, M. L. Becker, and M. Cakmak, Macromolecules **51**, 8114 (2018).

[68] See Supplemental Material at [link] for additional experimental details, a comparison of SAXS models, and representative POM videos.

[69] R. G. Larson, *The Structure and Rheology of Complex Fluids* (OUP USA, 1999).

[70] A SAXS/WAXS/GISAXS Beamline with Multilayer Monochromator. A. Hexemer, W. Bras, J. Glossinger, E. Schaible, E. Gann, R. Kirian, A. MacDowell, M. Church, B. Rude, and H. Padmore, Journal of Physics: Conference Series **247**, 012007 (2010).

[71] Real-Time Simultaneous Wide- and Small-Angle Fibre Diffraction. W. Bras, G. R. Mant, G. E. Derbyshire, W. J. O'Kane, W. I. Helsby, C. J. Hall, and A. J. Ryan, Journal of Synchrotron Radiation **2**, 87 (1995).

[72] Cooperative deformation of mineral and collagen in bone at the nanoscale. H. S. Gupta, J. Seto, W. Wagermaier, P. Zaslansky, P. Boesecke, and P. Fratzl, Proceedings of the National Academy of Sciences **103**, 17741 (2006).

[73] Characterization of the effects of x-ray irradiation on the hierarchical structure and mechanical properties of human cortical bone. H. D. Barth, E. A. Zimmermann, E. Schaible, S. Y. Tang, T. Alliston, and R. O. Ritchie, Biomaterials **32**, 8892 (2011).

[74] Collagen Fibril Alignment and Deformation during Tensile Strain of Leather: A Small-Angle X-ray Scattering Study. M. M. Basil-Jones, R. L. Edmonds, G. E. Norris, and R. G. Haverkamp, Journal of Agricultural and Food Chemistry **60**, 1201 (2012).

[75] Mechanical adaptability of the Bouligand-type structure in natural dermal armour. E. A. Zimmermann, B. Gludovatz, E. Schaible, N. K. N. Dave, W. Yang, M. A. Meyers, and R. O. Ritchie, Nature Communications **4**, 2634 (2013).

[76] On the tear resistance of skin. W. Yang, V. R. Sherman, B. Gludovatz, E. Schaible, P. Stewart, R. O. Ritchie, and M. A. Meyers, Nature Communications **6**, 6649 (2015).

[77] Novel Defense Mechanisms in the Armor of the Scales of the "Living Fossil" Coelacanth Fish. H. Quan, W. Yang, E. Schaible, R. O. Ritchie, and M. A. Meyers, Advanced Functional Materials **28**, 1804237 (2018).

[78] Nika: software for two-dimensional data reduction. J. Ilavsky, Journal of Applied Crystallography **45**, 324 (2012).

[79] Small-angle neutron scattering from typical synthetic and biopolymer solutions. F. Horkay and B. Hammouda, Colloid and Polymer Science **286**, 611 (2008).

[80] Thermoresponsive and Mechanical Properties of Poly(l-proline) Gels. M. Gkikas, R. K. Avery, and B. D. Olsen, Biomacromolecules **17**, 399 (2016).

[81] Origin of the scattering peak in microemulsions. M. Teubner and R. Strey, The Journal of Chemical Physics **87**, 3195 (1987).

[82] The Crystal Structure of a Five-Stranded Coiled Coil in COMP: A Prototype Ion Channel? V. N. Malashkevich, R. A. Kammerer, V. P. Efimov, T. Schulthess, and J. Engel, Science **274**, 761 (1996).

[83] Hydrodynamic Radii of Native and Denatured Proteins Measured by Pulse Field Gradient NMR Techniques. D. K. Wilkins, S. B. Grimshaw, V. Receveur, C. M. Dobson, J. A. Jones, and L. J. Smith, Biochemistry **38**, 16424 (1999).

[84] Dynamics of Entangled Solutions of Associating Polymers. M. Rubinstein and A. N. Semenov, Macromolecules **34**, 1058 (2001).

[85] Model Transient Networks from Strongly Hydrogen-Bonded Polymers. K. E. Feldman, M. J. Kade, E. W. Meijer, C. J. Hawker, and E. J. Kramer, Macromolecules **42**, 9072 (2009).

[86] The Influence of Hydrogen Bonding Side-Groups on Viscoelastic Behavior of Linear and Network Polymers. C. L. Lewis, K. Stewart, and M. Anthamatten, Macromolecules **47**, 729 (2014).

[87] Decoupling Bulk Mechanics and Mono- and Multivalent Ion Transport in Polymers Based on Metal–Ligand Coordination. N. S. Schauser, G. E. Sanoja, J. M. Bartels, S. K. Jain, J. G. Hu, S. Han, L. M. Walker, M. E. Helgeson, R. Seshadri, and R. A. Segalman, Chemistry of Materials **30**, 5759 (2018).

[88] Fractures in complex fluids: the case of transient networks. C. Ligoure and S. Mora, Rheologica Acta **52**, 91 (2013).

[89] Brittle fracture of polymer transient networks. S. Arora, A. Shabbir, O. Hassager, C. Ligoure, and L. Ramos, Journal of Rheology **61**, 1267 (2017).

[90] Rheology and Dynamics of Associative Polymers in Shear and Extension:□ Theory and Experiments. A. Tripathi, K. C. Tam, and G. H. McKinley, Macromolecules **39**, 1981 (2006).

[91] Delayed Fracture of an Inhomogeneous Soft Solid. D. Bonn, H. Kellay, M. Prochnow, K. Ben-Djemiaa, and J. Meunier, Science **280**, 265 (1998).

[92] Determination of orientation of the crystalline and amorphous phases in polyethylene by X-ray diffraction. Z. W. Wilchinsky, Journal of Polymer Science Part A-2: Polymer Physics **6**, 281 (1968).

[93] Quantitative evaluation of orientation in cellulose fibres from the X-ray fibre diagram. J. J. Hermans, P. H. Hermans, D. Vermaas, and A. Weidinger, Recueil des Travaux Chimiques des Pays-Bas **65**, 427 (1946).

[94] Drawing in poly(ε-caprolactone) fibers: tuning mechanics, fiber dimensions and surface-modification density. S.-E. Kim, A. M. Jordan, L. T. J. Korley, and J. K. Pokorski, Journal of Materials Chemistry B **5**, 4499 (2017).

[95] Oriented structure and anisotropy properties of polymer blown films: HDPE, LLDPE and LDPE. X. M. Zhang, S. Elkoun, A. Ajji, and M. A. Huneault, Polymer **45**, 217 (2004).

[96] Thermal and mechanical properties of injection molded liquid crystalline polymer/amorphous polymer blends. K. Engberg, O. Strömberg, J. Martinsson, and U. W. Gedde, Polymer Engineering & Science **34**, 1336 (1994).

[97] The Effect of Polymer Chain Alignment and Relaxation on Force-Induced Chemical Reactions in an Elastomer. B. A. Beiermann, S. L. B. Kramer, P. A. May, J. S. Moore, S. R. White, and N. R. Sottos, Advanced Functional Materials **24**, 1529 (2014).

[98] Relationship between birefringence and the structure of ordered block copolymer materials. N. P. Balsara, B. A. Garetz, and H. J. Dai, Macromolecules **25**, 6072 (1992).

[99] Birefringence and diffraction of light in ordered block copolymer materials. B. A. Garetz, M. C. Newstein, H. J. Dai, S. V. Jonnalagadda, and N. P. Balsara, Macromolecules **26**, 3151 (1993).

[100] The Poisson Ratio in Polymer Gels. E. Geissler and A. M. Hecht, Macromolecules **13**, 1276 (1980).

[101] Mechanical properties of hydrogels and their experimental determination. K. S. Anseth, C. N. Bowman, and L. Brannon-Peppas, Biomaterials **17**, 1647 (1996).

[102] Models for the specific adhesion of cells to cells. G. Bell, Science **200**, 618 (1978).

[103] Celebrating Soft Matter's 10th Anniversary: Chain configuration and rate-dependent mechanical properties in transient networks. M. K. Sing, Z.-G. Wang, G. H. McKinley, and B. D. Olsen, Soft Matter **11**, 2085 (2015).

[104] Elastic Breakup in Uniaxial Extension of Entangled Polymer Melts. Y. Wang, P. Boukany, S.-Q. Wang, and X. Wang, Physical Review Letters **99**, 237801 (2007).

[105] Simulation of Elastic Rupture in Extension of Entangled Monodisperse Polymer Melts. A. Lyhne, H. K. Rasmussen, and O. Hassager, Physical Review Letters **102**, 138301 (2009).

[106] Observing the chain stretch transition in a highly entangled polyisoprene melt using transient extensional rheometry. J. K. Nielsen, O. Hassager, H. K. Rasmussen, and G. H. McKinley, Journal of Rheology **53**, 1327 (2009).

[107] Molecular Tensile Machines: Anti-Arrhenius Cleavage of Disulfide Bonds. Y. Li, A. Nese, K. Matyjaszewski, and S. S. Sheiko, Macromolecules **46**, 7196 (2013).

[108] A facile mechanophore functionalization of an amphiphilic block copolymer towards remote ultrasound and redox dual stimulus responsiveness. R. Tong, X. Lu, and H. Xia, Chemical Communications **50**, 3575 (2014).

[109] Disulfide-centered poly(methyl acrylates): Four different stimuli to cleave a polymer. U. F. Fritze, S. L. Craig, and M. von Delius, Journal of Polymer Science Part A: Polymer Chemistry **56**, 1404 (2018).